Commun Nonlinear Sci Numer Simulat 85 (2020) 105181

Contents lists available at ScienceDirect

Commun Nonlinear Sci Numer Simulat

journal homepage: www.elsevier.com/locate/cnsns

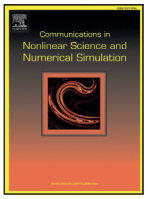

Research paper

Calcium buffers and L-type calcium channels as modulators of cardiac subcellular alternans

Yi Ming Lai, Stephen Coombes, Rüdiger Thul*

Centre for Mathematical Medicine and Biology, School of Mathematical Sciences, University of Nottingham, Nottingham NG7 2RD, UK

ARTICLE INFO

Article history:
Available online 8 February 2020

Keywords:
Calcium cycling
Synchrony
Luminal diffusion
Subcellular calcium alternans
Saddle-node bifurcation

ABSTRACT

In cardiac myocytes, calcium cycling links the dynamics of the membrane potential to the activation of the contractile filaments. Perturbations of the calcium signalling toolkit have been demonstrated to disrupt this connection and lead to numerous pathologies including cardiac alternans. This rhythm disturbance is characterised by alternations in the membrane potential and the intracellular calcium concentration, which in turn can lead to sudden cardiac death. In the present computational study, we make further inroads into understanding this severe condition by investigating the impact of calcium buffers and L-type calcium channels on the formation of subcellular calcium alternans when calcium diffusion in the cytosol is weak and the main route of Ca^{2+} transport in the myocyte is via the sarcoplasmic reticulum. Through numerical simulations of a two dimensional network of calcium release units, we show that increasing calcium entry is proarrhythmogenic and that this is modulated by the calcium-dependent inactivation of the L-type calcium channel. We also find that while calcium buffers can exert a stabilising force and abolish subcellular Ca^{2+} alternans, they can significantly shape the spatial patterning of subcellular calcium alternans. Taken together, our results demonstrate that subcellular calcium alternans can emerge via various routes and that calcium diffusion in the sarcoplasmic reticulum critically determines their spatial patterns.

1. Intoduction

Cardiac arrhythmias constitute a leading public health problem and cause most cases of sudden cardiac death. In the US alone, sudden cardiac death accounts for approximately 300,000–450,000 lives every year [1]. Among the many forms of cardiac arrhythmias, cardiac alternans feature prominently. This rhythm disturbance at the level of a single cardiac myocyte is characterised by alternating patterns of the membrane potential and the intracellular calcium (Ca^{2+}) concentration on successive beats. For instance, at one beat, a long action potential duration (APD) is accompanied by a large intracellular Ca^{2+} transient, while on the next beat, the APD is shortened concomitant with a small amplitude Ca^{2+} transient. As a consequence, contractile efficiency is impaired, which in turn can cause a detrimental reduction in blood flow. In early experimental studies, the intracellular Ca^{2+} concentration was averaged across a cardiac myocyte. The advent of high-resolution microscopy revealed that alternating Ca^{2+} dynamics were already present at individual Ca^{2+} release units (CRU)

* Corresponding author.
E-mail address: ruediger.thul@nottingham.ac.uk (R. Thul).

https://doi.org/10.1016/j.cnsns.2020.105181

[2–4]. While one CRU follows a pattern of large-small-large Ca^{2+} transients, neighbouring CRUs exhibit small-large-small Ca^{2+} transients. Crucially, both CRUs experience the same membrane potential. These findings gave rise to the concept of subcellular Ca^{2+} alternans [5–13] and illustrated that nonlinear processes govern cardiac dynamics across multiple scales: the cell wide membrane potential and the Ca^{2+} fluxes restricted to single dyadic clefts.

The existence of subcellular Ca^{2+} alternans reinforces the notion of cardiac myocytes as a network of networks. Each CRU can be conceptualised as a network of interacting components such as L-type Ca^{2+} channels, sodium-calcium exchangers (NCXs) and ryanodine receptors (RyRs). These local networks are then coupled via Ca^{2+} diffusion through both the cytosol and the sarcoplasmic reticulum (SR). This interconnectedness offers multiple explanations for the origin of subcellular Ca^{2+} alternans. On the one hand, we have previously shown [14] that Ca^{2+} alternans can emerge purely through coupling. In [14], we initially considered a coupled CRU network in which each node exhibited a regular period-1 orbit, i.e. the network mimicked a physiologically healthy state. Upon increasing the coupling strength between the nodes, i.e. decreasing τ_c in Eq. (1b), and *without* changing any other parameter values, we observed alternating solutions in which neighbouring CRUs oscillated out-of-phase. A key step in this study was the derivation of a map Γ that linked an initial perturbation of the CRU network δy_0 around the synchronous network state (which corresponds to the physiologically healthy state of the myocyte) to its final state δy_f after one pacing period: $\delta y_f = \Gamma \delta y_0$. We found that one eigenvalues of the matrix Γ exited the unit disk through -1 along the real axis upon decreasing τ_c, which is consistent with the subcellular Ca^{2+} alternans that we observed in direct numerical simulations of the CRU network. Crucially, the spatial patterns of the subcellular Ca^{2+} alternans may depend on whether Ca^{2+} diffusion is stronger in the cytosol or in the SR. In a recent model of Ca^{2+} cycling [15,16], Ca^{2+} alternans emerge for dominant cytosolic coupling via the traditional period-doubling bifurcation, where an eigenvalue of Γ leaves the unit disk at -1 along the real line. In addition to the findings in [14], we also observed subcellular Ca^{2+} alternans where different parts of the cell oscillate out-of-phase as seen experimentally in e.g. [8]. However, for dominant luminal coupling, there is a saddle-node bifurcation of the map Γ, where the leading eigenvalue leaves the unit disk at $+1$ along the real axis. In this case, each node follows a period-1 orbit, but the amplitudes of neighbouring CRUs varies. On the other hand, changes to the molecular components of a CRU can induce Ca^{2+} alternans, exemplified by weakening sarco-endoplasmic Ca^{2+} ATP (SERCA) pumps or increasing Ca^{2+} flux through L-type Ca^{2+} channels.

To date, investigations on how Ca^{2+} alternans emerge due to modifications at the CRU level have almost exclusively focussed on dominant cytosolic coupling [6,17–23]. However, the question as to whether Ca^{2+} diffusion in the SR is slow or fast — and hence weak or strong — is still unanswered [24–26]. Here, we focus on stronger SR Ca^{2+} diffusion in the presence of weak cytosolic Ca^{2+} diffusion and explore the impact of two modifiers of the local Ca^{2+} dynamics on the genesis of subcellular Ca^{2+} alternans: L-type Ca^{2+} channels and Ca^{2+} buffers.

The L-type Ca^{2+} channel has received significant attention due to its central role in excitation-contraction coupling [27–30]. Its contribution to the formation of Ca^{2+} alternans is ambiguous though [31]. On the one hand, several studies have provided compelling evidence that altering the dynamics of L-type Ca^{2+} channel through e.g. cooperative gating or reducing the current can either promote or inhibit Ca^{2+} alternans [32,33]. On the other hand, Ca^{2+} alternans have been observed with clamped membrane voltage, thus limiting the degree of control that L-type Ca^{2+} channels can exert on the genesis of Ca^{2+} alternans [34]. Here, we investigate the role of Ca^{2+}-dependent inactivation of the L-type Ca^{2+} channel on the dynamics of a CRU, which occurs in addition to voltage-dependent activation and inactivation [35,36]. We find that Ca^{2+}-dependent inactivation affects the formation of subcellular Ca^{2+} alternans in a nontrivial manner that depends on the unitary current of the L-type Ca^{2+} channel.

Ca^{2+} buffers are essential for cardiac function, not least because activation of the cytoplasmic buffer troponin C determines how strongly a cardiac myocyte contracts [27,37]. In addition, the buffers calsequestrin and calmodulin have been shown to vitally shape the dynamics of cardiac myocyte including an impact on the refractoriness of RyRs [38–52]. As has been demonstrated both experimentally and theoretically for numerous cell types and Ca^{2+} releasing channels, including the inositol-1,4,5-trisphosphate receptor, Ca^{2+} buffers can fundamentally alter the dynamics of intracellular Ca^{2+} dynamics ranging from local Ca^{2+} release events such as Ca^{2+} sparks and Ca^{2+} puffs to global Ca^{2+} patterns such as travelling Ca^{2+} waves. Due to the nonlinear dynamics of Ca^{2+} buffers, direct predictions are difficult to make. We show through numerical simulations that Ca^{2+} buffers can both promote and inhibit subcellular Ca^{2+} alternans, which adds another facet to the already rich repertoire of buffered Ca^{2+} dynamics.

2. Materials and methods

We consider a two-dimensional network of 15×10 CRUs corresponding to a transversal cut along a z-plane. We assume that CRUs are structurally identical, but note recent experimental evidence of heterogeneity amongst CRUs [53]. The dynamics of a CRU with label μ is governed by the Shiferaw-Karma model [34]

$$\frac{dc_s^\mu}{dt} = \beta(c_s^\mu)\left[\frac{\nu_i}{\nu_s}\left(I_r^\mu - \frac{c_s^\mu - c_i^\mu}{\tau_s} - I_{CaL}^\mu\right) + I_{NCX}^\mu\right], \tag{1a}$$

$$\frac{dc_i^\mu}{dt} = \beta(c_i^\mu)\left[\frac{c_s^\mu - c_i^\mu}{\tau_s} - I_{up}^\mu\right] + \sum_{\eta \in \mathcal{I}_n} \frac{c_i^\eta - c_i^\mu}{\tau_c}, \tag{1b}$$

$$\frac{\mathrm{d}c_{\mathrm{j}}^{\mu}}{\mathrm{d}t} = -I_{\mathrm{r}}^{\mu} + I_{\mathrm{up}}^{\mu} + \sum_{\eta\in\mathcal{I}_n} \frac{c_{\mathrm{j}}^{\eta} - c_{\mathrm{j}}^{\mu}}{\tau_{\mathrm{sr}}}\,, \tag{1c}$$

$$\frac{\mathrm{d}c_{\mathrm{u}}^{\mu}}{\mathrm{d}t} = \frac{c_{\mathrm{j}}^{\mu} - c_{\mathrm{u}}^{\mu}}{\tau_{\mathrm{a}}}\,, \tag{1d}$$

$$\frac{\mathrm{d}I_{\mathrm{r}}^{\mu}}{\mathrm{d}t} = -gI_{\mathrm{CaL}}Q\left(c_{\mathrm{u}}^{\mu}\right) - \frac{I_{\mathrm{r}}^{\mu}}{\tau_{\mathrm{r}}}\,. \tag{1e}$$

The Ca^{2+} concentrations in the subsarcolemmal space and in the cytosolic bulk are denoted by c_{s}^{μ} and c_{i}^{μ}, respectively, while the total Ca^{2+} concentration in the SR and the Ca^{2+} concentration in the unrecruited SR are given by c_{j}^{μ} and c_{u}^{μ}, respectively. The Ca^{2+} release current from the unrecruited SR into the subsarcolemmal space is I_{r}^{μ}, and we refer to the L-type Ca^{2+} current, the NCX current and the SERCA uptake current by I_{CaL}^{μ}, I_{NCX}^{μ} and I_{up}^{μ}, respectively. The model contains four diffusive currents with timescales τ_{s}, τ_{c}, τ_{sr} and τ_{a}, describing coupling between the subsarcolemmal space and the cytosolic bulk, through the cytosolic bulk between neighbouring CRUs (indexed by $\mathcal{I}_n$), between the total and unrecruited SR, and through the SR between neighbouring CRUs (indexed by $\mathcal{I}_n$), respectively. Note that each CRU is coupled to its four nearest neighbours. In some instances, we report the network coupling strengths as inverse of the timescales, i.e. $\sigma_x = \tau_x^{-1}$, $x \in \{\mathrm{c}, \mathrm{sr}\}$. The L-type Ca^{2+} current is modelled as $I_{\mathrm{CaL}}^{\mu} = I_{\mathrm{Ca}}^{\mu} P_o$ with

$$I_{\mathrm{Ca}}^{\mu} = 4i_{\mathrm{Ca}}P_{\mathrm{Ca}}F\alpha\frac{c_{\mathrm{s}}^{\mu}\times 10^{-3}\exp(2\alpha) - \gamma_0\mathrm{Ca}_o}{\exp(2\alpha-1)}\,, \tag{2}$$

where $\alpha = FV/RT$, i_{Ca} is the parameter that we vary to control the strength of the L-type Ca^{2+} current and $P_o = dqf$ is the open probability. Here, d is the value of the fast voltage-dependent activation gate, q corresponds to the Ca^{2+}-dependent inactivation gate and f to the voltage-dependent inactivation gate. All gates are described by first order kinetics of the form

$$\frac{\mathrm{d}x}{\mathrm{d}t} = \frac{x_\infty - x}{\tau_x}\,, \qquad x \in \{d, f, q\}\,. \tag{3}$$

Of particular interest for the present study is

$$q_\infty = \frac{c_{\mathrm{e}}^{\gamma}}{c_{\mathrm{e}}^{\gamma} + c_{\mathrm{s}}^{\gamma}}\,, \tag{4}$$

where c_{e} sets the EC_{50} value, i.e. the value of the subsarcolemmal Ca^{2+} concentration c_{s} at which q_∞ equals 0.5, and γ controls the sensitivity of Ca^{2+}-dependent inactivation. Essentially, the larger γ the more step-like the inactivation around a Ca^{2+} concentration of c_{e}. Following [34], we clamp the voltage for a pacing period T_p as

$$V(t) = \begin{cases} V_+(t)\,, & kT_p \le t \le (k+x)T_p\,, \\ V_{\min}\,, & (k+x)T_p \le t < (k+1)T_p\,, \end{cases} \tag{5}$$

where $k \in \mathbb{N}$ counts the number of APs in the simulation and $x = a_x/(a_x + T_p)$ with $a_x = 2/3$. The resting potential is given by $V_{\min} = -70\mathrm{mV}$, and $V_+(t)$ captures the shape of the clamped voltage, which is given by

$$V_+(t) = V_{\min} + (V_{\max} - V_{\min})\sqrt{1 - \left(\frac{t - kT_p}{xT_p}\right)^2}\,. \tag{6}$$

Note that Eq. (6) is valid for $kT_p \le t \le (k+x)T_p$ and that each CRU experiences the same voltage. The maximal AP is set at $V_{\max} = 30\mathrm{mV}$. Buffering is modelled based on the fast-buffer approximation [54,55] yielding

$$\frac{1}{\beta(c)} = 1 + \frac{B_{\mathrm{SR}}K_{\mathrm{SR}}}{(c+K_{\mathrm{SR}})^2} + \frac{B_{\mathrm{T}}K_{\mathrm{T}}}{(c+K_{\mathrm{T}})^2} + \frac{B_{\mathrm{Cd}}K_{\mathrm{Cd}}}{(c+K_{\mathrm{Cd}})^2}\,, \tag{7}$$

where B_{SR} denotes the total buffer concentration in the SR and K_{SR} the associated dissociation constant. Constants with the subscript T and Cd have the same interpretation, but correspond to troponin C and calmodulin, respectively. For all other details of the model including the functional forms i_{Ca} and I_{NCX}, we refer the reader to [34]. A list of all parameter values used in this study is provided in Table 1. We employ no-flux boundary conditions in all simulations.

3. Results

As this study focuses on subcellular Ca^{2+} alternans in two-dimensional CRU networks, we wish to visualise the Ca^{2+} concentration simultaneously across the two spatial dimensions and time. One way to achieve this is illustrated in Fig. 1 for a 5×3 CRU network. On the left, we plot one component of the CRU model, e.g. the subsarcolemmal Ca^{2+} concentration or

Table 1
Standard parameter values used in the study.

	Definition	Value
T	Temperature	308 K
F	Faraday's constant	96.4867 C/mmol
R	Gas constant	8.314 J/K mol
Na_o	External sodium concentration	140 mM
Ca_o	External calcium concentration	1.8 mM
v_s/v_i	Subsarcolemmal/cell volume	0.1
c_{up}	Uptake threshold	0.5 μM
v_{up}	Uptake strength	270 μM/s
$\bar{I}_{NaCa}$	Strength of the NaCa exchanger	10^5 μM/s
k_{sat}	Constant from the 1994 Luo-Rudy model	0.1
ξ	Constant from the 1994 Luo-Rudy model	0.35
K_{mNa}	Constant from the 1994 Luo-Rudy model	87.5 mM
K_{mCa}	Constant from the 1994 Luo-Rudy model	1.38 mM
γ_s	Constant from the 1994 Luo-Rudy model	1
γ_o	Constant from the 1994 Luo-Rudy model	0.341
P_{Ca}	Constant from the 1994 Luo-Rudy model	5.4×10^{-4} cm/s
i_{Ca}	Flux constant	6600 μmol/C cm
τ_f	Time constant for voltage-dependent inactivation	30 ms
τ_d	Time constant for voltage-dependent activation	5 ms
τ_q	Time constant for Ca^{2+}-dependent inactivation	20 ms
$\tilde{c}_C$	Calcium inactivation threshold	0.5 μM
γ	Sensitivity parameter for calcium dependent inactivation	4
g	Release current strength	3.5×10^4 sparks/μM
u	Release slope	11.3 s^{-1}
τ_r	Average spark life time	20 ms
τ_a	Relaxation time of c_u to c_j	50 ms
τ_s	Submembrane diffusion time constant	10 ms
B_T	Total concentration of troponin C binding sites	70 μmol/1 cytosol
B_{SR}	Total concentration of SR binding sites	47 μmol/1 cytosol
B_{Cd}	Total concentration of calmodulin binding sites	24 μmol/1 cytosol
K_T	Dissociation constant for troponin C binding sites	0.6 μM
K_{SR}	Dissociation constant for SR binding sites	0.6 μM
K_{Cd}	Dissociation constant for calmodulin binding sites	7 μM
β_s	Buffering constant for c_s	0.5
β_i	Buffering constant for c_i	0.01
σ_c	Coupling strength in cytosol	1 s^{-1}
σ_c	Coupling strength in the SR	30 s^{-1}

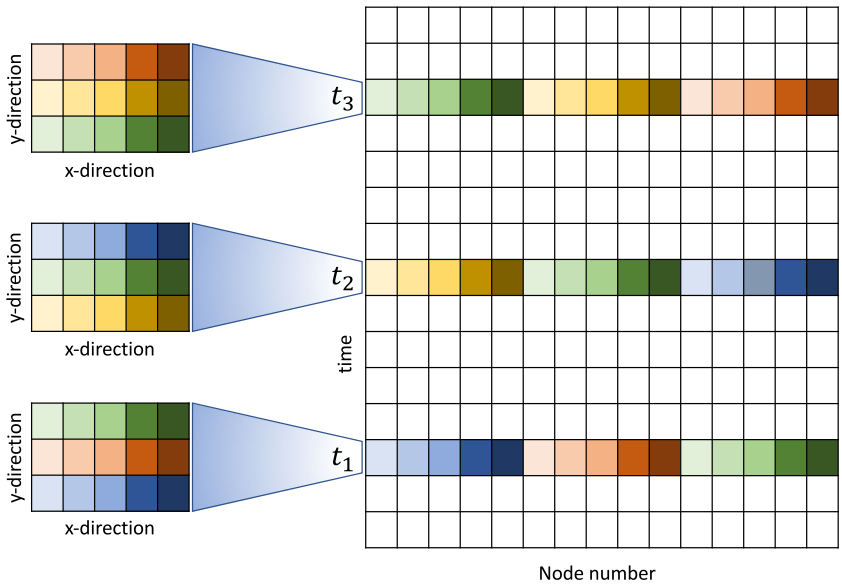

Fig. 1. Schematic showing the spatio-temporal visualisation of Ca^{2+} concentrations across a 5×3 CRU network. The three networks on the left represent the Ca^{2+} concentration for one node component of the CRU network at three different times $t_1 < t_2 < t_3$. The right plot corresponds to a space-time plot where space runs horizontally (represented as node number) and time vertically. See text for details.

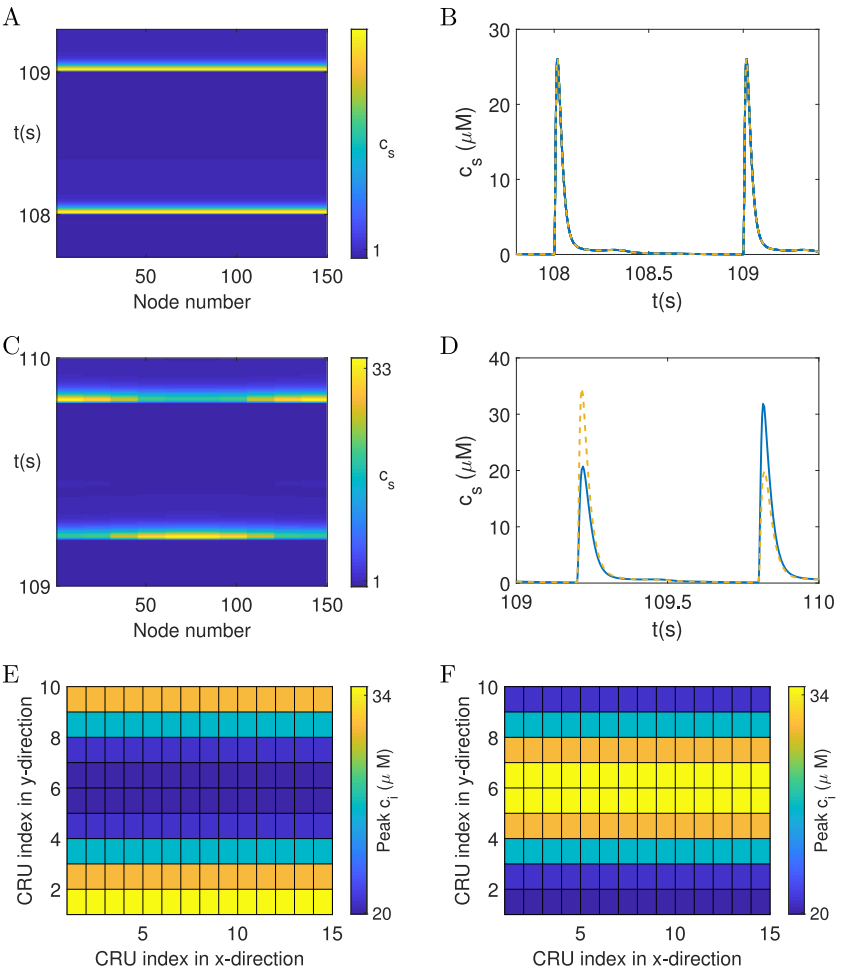

Fig. 2. Space-time plots of the unravelled CRU network (A,C) and time traces (B,D) of the subsarcolemmal Ca^{2+} concentration for $T_p = 1$ s (A,B) and $T_p = 0.6$ s (C,D). The colouring in (B,D) refers to node 25 (solid blue) and 75 (dashed yellow). (E,F) Peak subsarcolemmal Ca^{2+} concentration on two successive beats across the CRU network for the data shown in (C). Parameter values as in Table 1 and $\sigma_c = 15\ s^{-1}$, $\sigma_{sr} = 3\ s^{-1}$. (For interpretation of the references to colour in this figure legend, the reader is referred to the web version of this article.)

the Ca^{2+} concentration in the cytosolic bulk, at different times $t_1 < t_2 < t_3$. Each coloured box corresponds to one CRU, and the colour encodes the value of the CRU component. Note that the colour scheme is chosen for illustrative purposes only.

Each snapshot of the two-dimensional CRU network can be transformed into a one-dimensional representation by sequentially taking rows of the two-dimensional network from bottom to top and concatenating them horizontally from left to right. For instance, consider the network state at time t_1 shown on the left. We first take the row at the bottom (blue colours), which we amend from the right with the second row (orange colours) followed by the top row (green colours) to obtain the one-dimensional representation shown on the right. The order of elements within each row of the two-dimensional CRU network is conserved, as indicated by the same order of colours within each block of the same base colour, i.d. blue, orange and green. These one-dimensional representation are then stacked vertically to produce a space-time plot as shown on the right of Fig. 1. Here, space runs horizontally, represented as node number, and time runs from bottom to top. The node number is assigned by enumerating CRUs sequentially starting with the bottom left CRU in the two-dimensional network. We then proceed along the row towards the right increasing the node number by one until we reach the end of that row. We then continue with the left-most CRU in the next row above, again moving left to right.

To establish a baseline for our findings, we first investigate the dynamics of the CRU network when buffers are clamped over time. In other words, we set $\beta(c_s^\mu) \equiv \beta_s = \text{const}$ and $\beta(c_i^\mu) \equiv \beta_i = \text{const}$ for all μ. When cytosolic coupling is dominant, i.e. $\tau_c \ll \tau_{sr}$ ($\sigma_c \gg \sigma_{sr}$), synchrony is stable for low pacing frequencies as demonstrated in Fig. 2A. We here show a space-time plot of the *unravelled* CRU network as introduced above. The existence of stable synchronous network solutions can be inferred from these representations by the absence of any horizontal variation in colouring: each CRU exhibits identical behaviour. Fig. 2B makes this explicit by showing the temporal evolution of the subsarcolemmal Ca^{2+} concentration at nodes 25 and 75. The two curves lie on top of each other. The results in Fig. 2 as well as all other data presented in this study

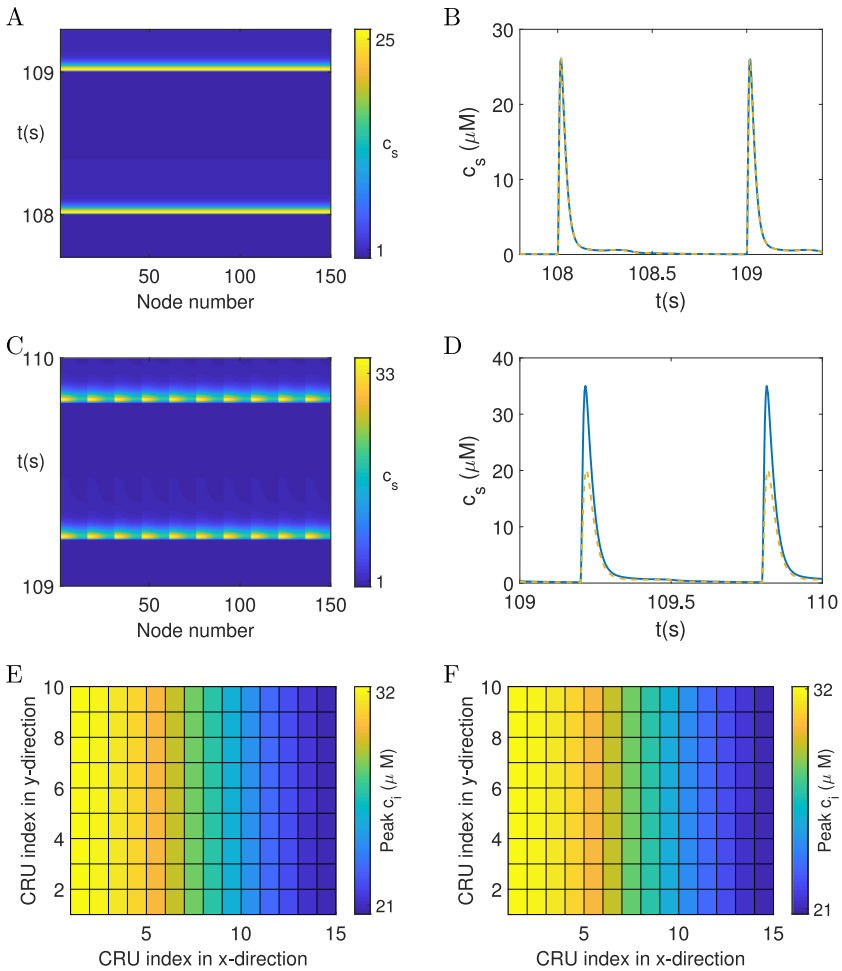

Fig. 3. Space-time plots of the unravelled CRU network (A,C) and time traces (B,D) of the subsarcolemmal Ca^{2+} concentration for $T_p = 1$ s (A,B) and $T_p = 0.6$ s (C,D). The colouring in (B,D) refers to node 31 (solid blue) and 75 (dashed yellow). (E,F) Peak subsarcolemmal Ca^{2+} concentration on two successive beats across the CRU network for the data shown in (C). Parameter values as in Table 1 and $\sigma_c = 2$ s^{-1}, $\sigma_{sr} = 30$ s^{-1}. (For interpretation of the references to colour in this figure legend, the reader is referred to the web version of this article.)

are obtained after a sufficiently long simulation time so that initial transients have decayed and the system is at steady state. For instance, the data in Fig. 2A depicts the subsarcolemmal Ca^{2+} concentration for beats 181 and 182. When we decrease T_p, we observe the emergence of subcellular Ca^{2+} alternans as depicted in Fig. 2C. Each CRU follows a period-2 orbit, where a small amplitude Ca^{2+} transient on one beat is followed by a large Ca^{2+} transient on the next beat. Consider the node with number 75. During the first stimulus (around 109.2 s) we observe a large transient indicated by the yellow colour. On the next beat at around 109.8 s, the same node exhibits a much smaller transient as can be gleaned from the bluish colour. The behaviour is reversed for node 25, which first exhibits a small amplitude transient, followed by a large amplitude transient. This is shown explicitly in Fig. 2D, where we again plot the time traces of the subsarcolemmal Ca^{2+} concentration at these two nodes. Fig. 2E and F provide a more detailed view on the emergent spatial Ca^{2+} pattern. We plot the peak subsarcolemmal Ca^{2+} concentration on two successive beats. Since CRUs obtain their individual maximal values at the same time during one beat, Fig. 2E and F correspond to snapshots of the subsarcolemmal Ca^{2+} concentration across the entire CRU network at these maximal peak times. The Ca^{2+} alternans are arranged in an *inside-out* pattern along the long axis of the network, where CRUs within one row show almost identical behaviour, but peak amplitudes vary along the vertical direction. When Ca^{2+} transients are large in the centre, they are small towards the top and bottom. On the next beat, this pattern is reversed with large Ca^{2+} transients at the top and bottom.

For dominant luminal coupling, where $\tau_c \gg \tau_{sr}$ ($\sigma_c \ll \sigma_{sr}$), we again find stable synchrony at low pacing frequencies (see Fig. 3A and B). Indeed, the space-time plot and the time traces of the subsarcolemmal Ca^{2+} concentration are identical to the those in Fig. 2A and B, since when all CRUs exhibit the same behaviour, the coupling terms in Eqs. (1b) and (1c) vanish. The main difference between dominant cytosolic and dominant luminal coupling becomes apparent when we lower T_p. For the latter, we find subcellular Ca^{2+} alternans that emerge via a saddle-node bifurcation at the network level, in contrast to

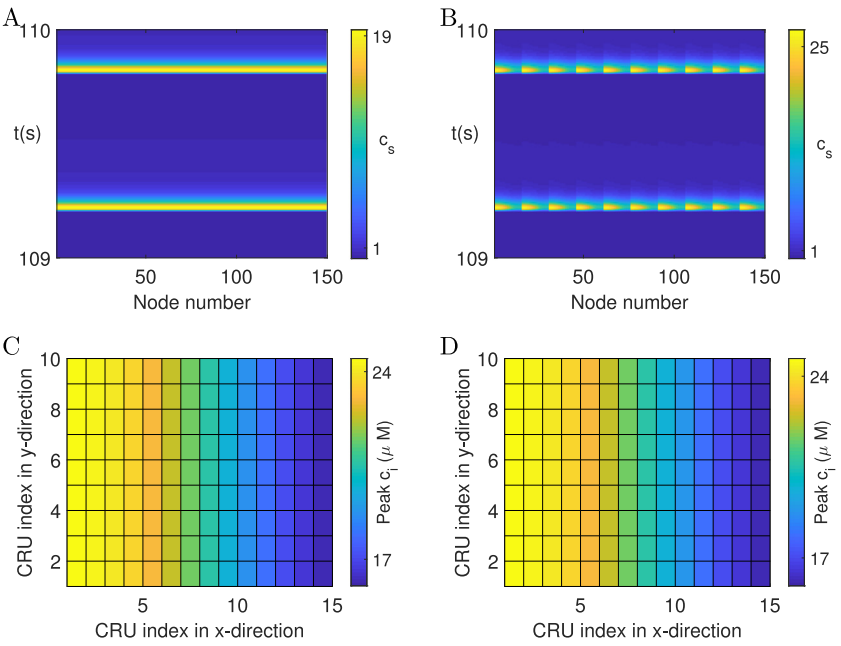

Fig. 4. Space-time plot of the subsarcolemmal Ca^{2+} concentration of the unravelled CRU network for $i_{Ca} = 4400$ μmol $C^{-1}cm^{-1}$ and (A) $\gamma = 1$, (B) $\gamma = 3$. (C,D) Peak subsarcolemmal Ca^{2+} concentration on two successive beats across the CRU network. Parameter values as in (B). For all other parameter values, see Table 1.

a period doubling bifurcation for the former. As Fig. 3C and D highlight, each CRU follows a period-1 orbit, but this orbit differs amongst the CRUs in the network. Fig. 3E and F show the peak subsarcolemmal Ca^{2+} concentration during one beat across the CRU network and illustrate that CRUs on the left form large Ca^{2+} amplitude transients, while the transients are smaller towards the right. In the following we will use Fig. 3C–F as a reference case and contrast them with the network behaviour when we alter the behaviour of the L-type Ca^{2+} channel and that of Ca^{2+} buffers.

3.1. *L-type* Ca^{2+} *channel*

The extent to which Ca^{2+}-dependent inactivation sets in as a function of the subsarcolemmal Ca^{2+} concentration c_s^μ is controlled by the exponent γ in Eq. (4). When γ is small, the inverse Hill function q_∞ drops slowly from 1 to 0, while a large value of γ leads to switch-like behaviour around a concentration value of c_e. As Fig. 4A illustrates, the synchronous network state is stable when γ is small. On the other hand, as γ is increased, subcellular Ca^{2+} alternans emerge via a saddle-node bifurcation as shown in Fig. 4B–D. Fig. 4B displays a space-time plot of the unravelled CRU network where the variation of the maxima of the Ca^{2+} transients is clearly visible as the colour changes from yellow to blue when we traverse the network. We can also discern changes in the duration of the Ca^{2+} transient as evidenced by the wedge shape of the yellow regions of increased Ca^{2+}. Fig. 4C and D provide more detail on the spatial pattern of the subcellular Ca^{2+} alternans. On each beat, large Ca^{2+} transients occur towards the left side of the myocyte, while Ca^{2+} transients are small towards the right side. Note that there is no variation of the Ca^{2+} peak amplitudes along the y-direction. These results suggest that a more gradual Ca^{2+}-dependent inhibition of the L-type Ca^{2+} channel, i.e. when γ is small, protects cardiac myocytes from subcellular Ca^{2+} alternans.

The unitary current of an L-type Ca^{2+} channel can be modulated through various mechanisms, including β-adrenergic stimulation. The space-time plot in Fig. 5A shows that for small values of i_{Ca}, synchrony is stable. However, upon increasing the single channel current, subcellular Ca^{2+} alternans emerge via a saddle-node bifurcation as illustrated in Fig. 5B. The Ca^{2+} pattern is identical to the one found in Fig. 4 in that the Ca^{2+} concentration remains constant vertically but varies horizontally, see Fig. 5C and D. The fact that the large Ca^{2+} transients occur towards the right in Fig. 5C and D as apposed to the left in Fig. 4C and D is due to initial conditions. Overall, the results plotted in Fig. 5 are consistent with experimental findings that upregulation of the L-type Ca^{2+} channel is pro-arrhythmogenic [33].

The Ca^{2+} profiles depicted in Figs. 4 and 5 suggest that the effect of the unitary L-type Ca^{2+} current on the generation of subcellular Ca^{2+} alternans depends on the properties of Ca^{2+}-dependent inactivation of the channel and vice versa. In Fig. 6 we provide a more comprehensive view on the interplay between these two components. For a given pair of γ and i_{Ca}, we compute the maximal difference in peak subsarcolemmal Ca^{2+} on successive beats for a CRU with index μ, i.e

$$\theta^\mu = \max_i \left| c_s^{\mu,i} - c_s^{\mu,i+1} \right|, \tag{8}$$

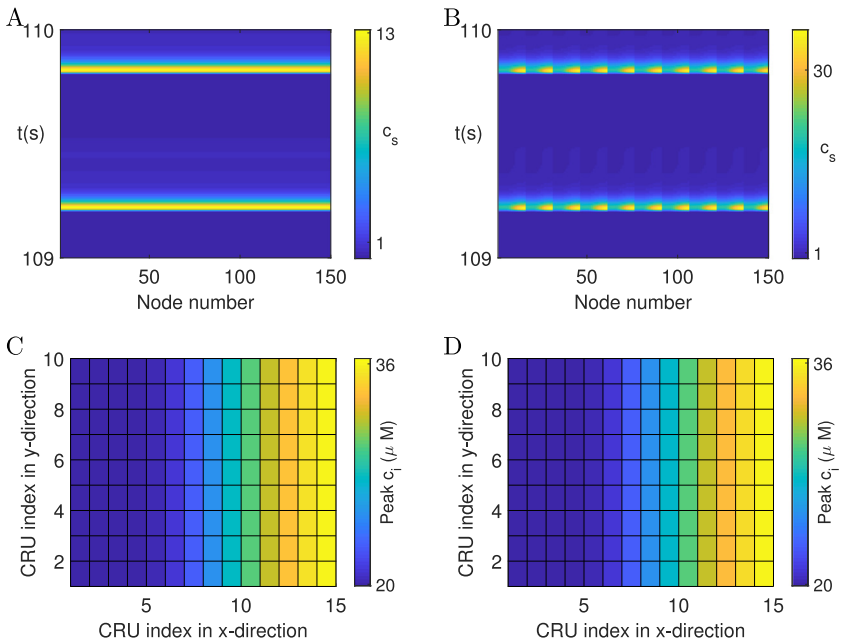

Fig. 5. Space-time plot of the subsarcolemmal Ca^{2+} concentration of the unravelled CRU network for $\gamma = 3$ and (A) $i_{Ca} = 2200$ μmol C^{-1}cm^{-1}, (B) $i_{Ca} = 6600$ μmol C^{-1}cm^{-1}. (C,D) Peak subsarcolemmal Ca^{2+} concentration on two successive beats across the CRU network. Parameter values as in (B). For all other parameter values, see Table 1.

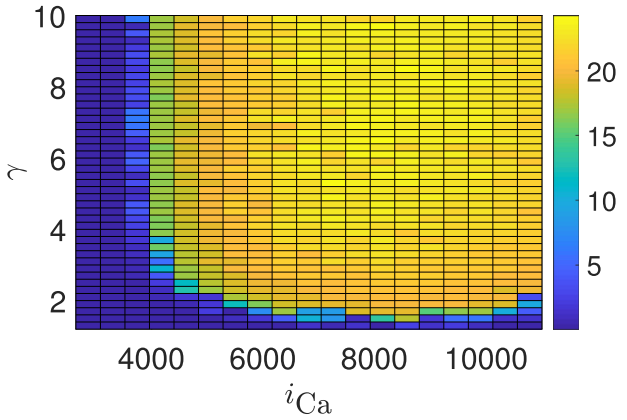

Fig. 6. Maximal beat-to-beat variation θ of the subsarcolemmal Ca^{2+} concentration as a function of γ and i_{Ca}. All other parameter values as in Table 1.

where $c_s^{\mu,i}$ is the maximum of c_s^{μ} on the ith beat. Then, we determine the maximum of all θ^{μ} across the CRU network, $\theta = \max_{\mu} \theta^{\mu}$. When i_{Ca} is small, θ vanishes irrespective of the value of γ, indicating that synchrony is stable and does not depend on how quickly Ca^{2+}-dependent inactivation sets in. For larger values of i_{Ca}, we observe a sharp transition from synchrony (blue) to alternans (yellow) upon increase of γ. Hence, for a sufficiently strong unitary L-type Ca^{2+} current, subcellular Ca^{2+} alternans can be induced if Ca^{2+}-dependent inactivation becomes more switch-like. When Ca^{2+}-dependent inactivation sets in more gradually, i.e. γ is small, synchrony is stable as we increase i_{Ca}. However, for larger values of γ, we observe a sharp transition from synchrony to subcellular Ca^{2+} alternans as the L-type Ca^{2+} channel becomes stronger. There appears to be an L-shape stability boundary in that for a large range of γ, subcellular Ca^{2+} alternans appear for approximately the same value of i_{Ca}, while for a large range of i_{Ca}, alternans set in for approximately the same small value of γ. We also note that the transition from stable synchrony to subcellular Ca^{2+} alternans is quite abrupt, as indicated by the sharp transition from blue to yellow. Taken together, our findings provide strong evidence that the L-type Ca^{2+} channel can initiate subcellular Ca^{2+} alternans, either via its Ca^{2+}-dependent inactivation or the strength of its unitary Ca^{2+} current.

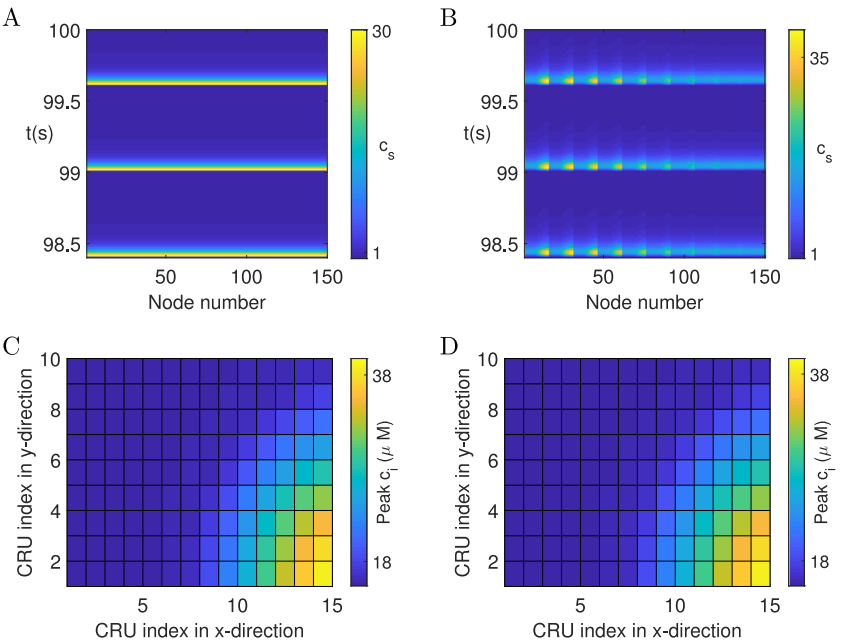

Fig. 7. Space-time plot of the subsarcolemmal Ca^{2+} concentration of the unravelled CRU network for (A) fully nonlinear buffers and (B) desensitised buffers. (C,D) Peak subsarcolemmal Ca^{2+} concentration on two successive beats across the CRU network. Parameter values as in (B). Other parameter values as in Table 1 and $K_{SR} = 6.0$ μM, $K_T = 600.0$ μM, $K_{Cd} = 7.0$ μM, $B_{SR} = 250.0$ μmol/l cytosol, $B_T = 12000.0$ μmol/l cytosol, $B_{Cd} = 1.0$ μmol/l cytosol.

4. Buffers

All results so far were obtained for constant buffer contributions. In other words, we set $\beta(c_i^\mu)$ and $\beta(c_s^\mu)$ to constants β_i and β_s, respectively, consistent with earlier work [14]. In this way, we eliminate any time-dependent modulation of the Ca^{2+} dynamics through binding and unbinding to Ca^{2+} buffers. Under more general conditions, however, Eq. (7) entails that $\beta(c_i^\mu)$ and $\beta(c_s^\mu)$ oscillate with the same frequency as c_i^μ and c_s^μ, respectively. Fig. 7A illustrates that in this case, subcellular Ca^{2+} alternans can be abolished and synchrony is stable. This behaviour needs to be contrasted with that depicted in Fig. 5B, which we would obtain with the parameter values used in Fig. 7A upon replacing the dynamic buffers with the constant buffers used in Fig. 5B. In other words, while the dynamics of the L-type Ca^{2+} channel can induce subcellular Ca^{2+} alternans (as demonstrated in Fig. 5), dynamic Ca^{2+} buffers can rescue this pathological behaviour. This discrepancy between constant and time-dependent buffers prompted us to explore another form of non-responsive buffers. The sensitivity of buffers is usually determined by their dissociation constants, which in the present study are the three constants K_{SR}, K_{Cd} and K_T in Eq. (7), as well as the corresponding concentration of binding sites B_{SR}, B_{Cd} and B_T. By choosing appropriate values, we can effectively "desensitise" the Ca^{2+} buffers. As Fig. 7B–D illustrate for the desensitised dynamics, subcellular Ca^{2+} alternans re-emerge consistent with a saddle-node bifurcation. Fig. 7B shows a space-time plot of the unravelled CRU network. Each CRU follows a period-1 orbit, which differs both in amplitude and duration of the Ca^{2+} transient across the network, as can be deduced from the variation of the yellow wedges. A more detailed view on the spatial pattern is provided in Fig. 7C and D, which depict peak amplitudes of the subsarcolemmal Ca^{2+} concentration on successive beats. Note that although the subcellular Ca^{2+} alternans emerge through a saddle-node bifurcation, the spatial pattern differs from that observed in Figs. 4 and 5. This is consistent with our earlier findings, which have demonstrated a rich pattern space of subcellular Ca^{2+} alternans [15,16].

At this point, one might be tempted to conclude that constant buffers make the occurrence of subcellular Ca^{2+} alternans more likely. However, as Fig. 8A reveals, this is not the case. Leaving all parameter values unchanged but setting $\beta_s = \beta_i = 1$ we find synchrony. Crucially, these simulations correspond to the case without buffers and should be contrasted with the results in Fig. 7A. In both cases, synchrony is stable, but the reasons as to why might differ. The constant values for β_s and β_i that we used in Section 3.1 were obtained for a piecewise linear (PWL) caricature of the model given by Eq. (1), see [14] for details. To obtain estimates that are more consistent with the full nonlinear model, we determine the mean values of $\beta(c_s^\mu)$ and $\beta(c_i^\mu)$ when synchrony is stable and assign them to β_s and β_i, respectively. For these values, we find subcellular Ca^{2+} alternans that are consistent with a saddle-node bifurcation as shown in Fig. 8B. Again, individual CRUs display a period-1 orbit, which differs throughout the network. The spatial pattern of the subcellular Ca^{2+} alternans is reminiscent of the one depicted in Fig. 4B–D, where Ca^{2+} transients are more pronounced on the left side of the CRU network compared to the right side.

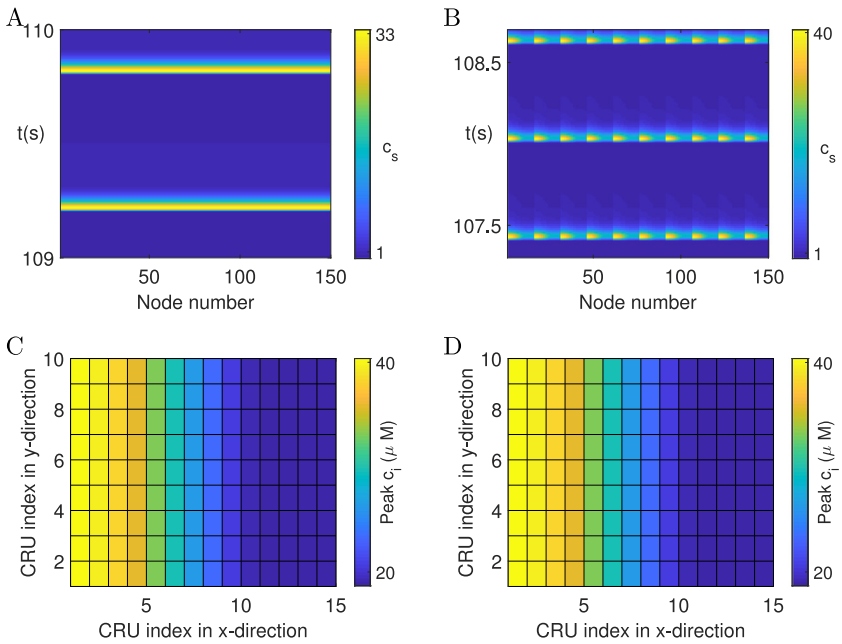

Fig. 8. Space-time plot of the subsarcolemmal Ca^{2+} concentration of the unravelled CRU network for $T_p = 0.6$ s and (A) $\beta_s = \beta_i = 1$, (B) $\beta_s = 0.08827$, $\beta_i = 0.01738$. (C,D) Peak subsarcolemmal Ca^{2+} concentration on two successive beats across the CRU network. Parameter values as in (B). For all other parameter values, see Table 1.

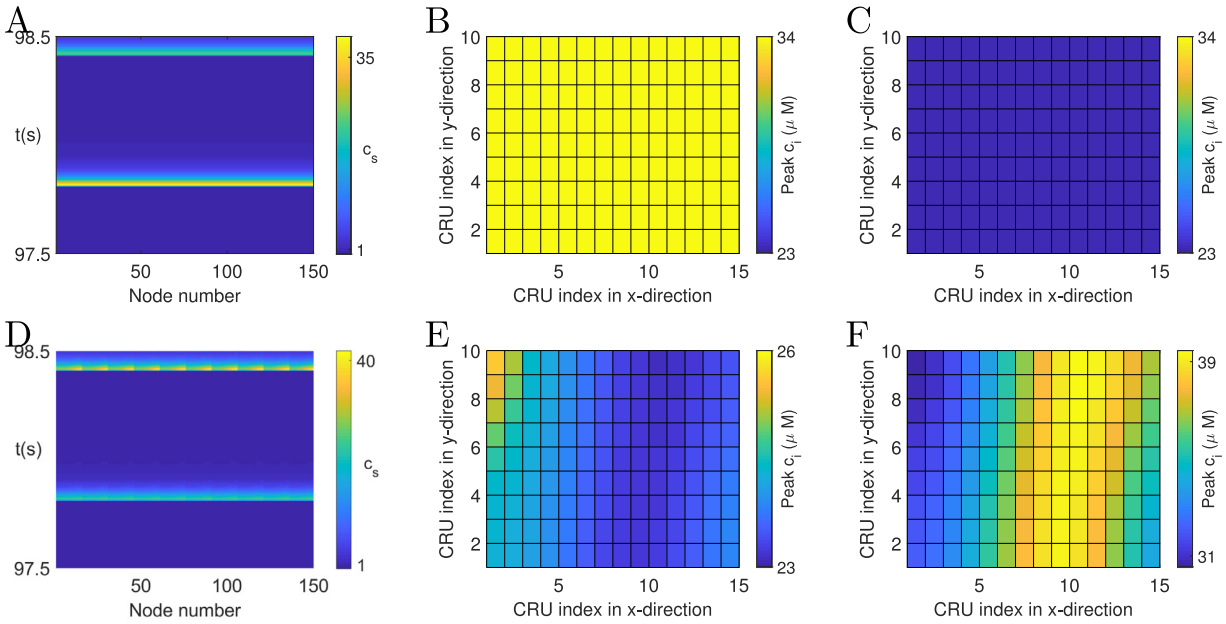

Fig. 9. Network dynamics for $T_p = 0.6$ s and clamped nonlinear buffers for (A–C) $\sigma_{sr} = 30\ s^{-1}$, $\sigma_c = 1\ s^{-1}$, (D–F) $\sigma_{sr} = 3\ s^{-1}$, $\sigma_c = 0\ s^{-1}$. Space-time plots of the subsarcolemmal Ca^{2+} concentration of the unravelled CRU are shown in (A) and (D). Peak subsarcolemmal Ca^{2+} concentration on two successive beats across the CRU network are plotted in (B,C) and (E,F). For all other parameter values, see Table 1.

Since constant Ca^{2+} buffers can both promote as well as abolish subcellular Ca^{2+} alternans, we next explore the impact of the buffer time course on the formation of subcellular Ca^{2+} alternans. To do this in a controlled fashion, we extract the time course of both $\beta(c_s^\mu)$ and $\beta(c_i^\mu)$ from the full nonlinear model and then clamp the buffer time courses at each node to these profiles. In other words, each node experiences nonlinear buffer dynamics, but the buffers do not alternate from node to node. As Fig. 9A reveals, we obtain subcellular Ca^{2+} alternans that differ from those reported so far in this study. Here, every node in the network follows the same period-2 orbit characteristic of subcellular Ca^{2+} alternans that

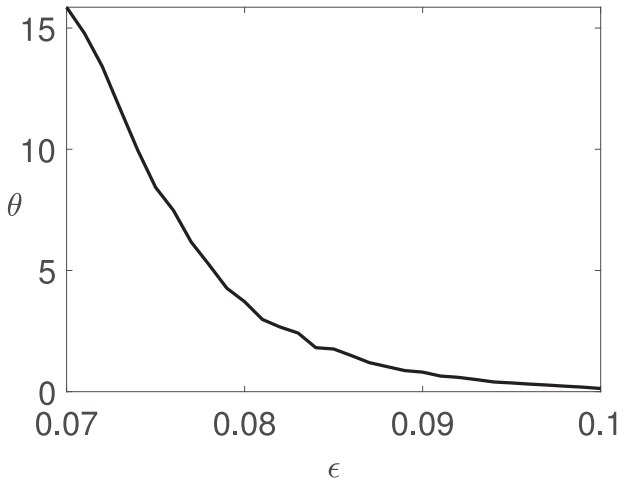

Fig. 10. Maximal beat-to-beat variation θ of the subsarcolemmal Ca^{2+} concentration as a function of the variability of the Ca^{2+} buffer ε. See text for details. Parameter values as in Table 1.

emerge via a period-doubling bifurcation. Fig. 9B and C illustrate the uniform behaviour across the network that alternates between successive beats. This spatial pattern is known as spatially concordant Ca^{2+} alternans. When we change the coupling strengths, but keep all other parameter values unaltered, we observe spatially discordant Ca^{2+} alternans as plotted in Fig. 9D–F. Every node follows a period-2 orbit, but different parts of the network oscillate out-of-phase with each other.

Our results so far strongly suggest that the time course and amplitude of Ca^{2+} buffers significantly impacts on the genesis of subcellular Ca^{2+} alternans. Fig. 10 shows results from an *in silico* experiment in which we tune the Ca^{2+} buffer dynamics from constant ($\varepsilon = 0$) to fully nonlinear ($\varepsilon = 1$) by replacing the buffer factor β in Eqs. (1a) and (1b) with

$$\beta_x^{\varepsilon} = \varepsilon\beta(c_x) + (1-\varepsilon)\beta_x\,, \qquad x \in \{x, i\}\,, \tag{9}$$

with $\beta(c_x)$ as in Eq. (7) and β_x as in Table 1. As a measure for the strength of subcellular Ca^{2+} alternans, we report the maximal beat-to-beat variation θ as defined after Eq. (8). As ε increases, we find a monotonic decrease in θ, highlighting that nonlinear buffers have the potential to abolish subcellular Ca^{2+} alternans.

5. Discussion

Subcellular Ca^{2+} alternans have been firmly linked to the genesis of cardiac arrhythmias. Despite this crucial connection, we still lack a complete picture of how the dynamics of the intracellular Ca^{2+} concentration transitions from its healthy period-1 orbit to its various pathological forms.

Our focus has been on understanding subcellular Ca^{2+} alternans in tubulated myocytes, such as ventricular myocytes. The presence of t-tubules in these cells gives rise to well-defined CRUs, which form a network where nearest neighbours are coupled via Ca^{2+} diffusion, both through the cytosol and the SR. The discussion of whether Ca^{2+} diffusion in the SR is fast or slow has been ongoing for more than a decade [24–26], without a resolution in sight. We illustrate in Figs. 2 and 3 that whether Ca^{2+} diffuses more dominantly in the lumen or in the cytosol has major consequences for the spatial patterns of subcellular Ca^{2+} alternans. In the latter, subcellular Ca^{2+} alternans emerge via the classical period-doubling bifurcation, where CRUs exhibit a period-2 orbit and CRUs in different parts of the cell oscillate out-of-phase with each other. This behaviour has been well studied and documented [5–12]. On the other hand, when Ca^{2+} diffusion in the SR dominates, we observe a completely different spatial pattern originating from a saddle-node bifurcation. Here, CRUs show a period-1 orbit, which is different from the synchronous network state and where CRUs in different regions of the cell exhibit Ca^{2+} transients of varying amplitude. It is worth noting that the discussion of whether intraluminal Ca^{2+} diffusion is faster than cytosolic Ca^{2+} diffusion — a process known as intraluminal tunnelling — has already received attention, although in a different context [56]. Given the largely unexplored nature of the saddle-node bifurcation in the generation of subcellular Ca^{2+} alternans, we have concentrated on dominant luminal coupling in the present study and have investigated two main contributors that shape the dynamics of cardiac Ca^{2+}: the L-type Ca^{2+} channel and Ca^{2+} buffers.

The L-type Ca^{2+} channel constitutes a major Ca^{2+} conduit that regulates Ca^{2+} influx from the extracellular space into the myoplasm and is thus crucial for high-fidelity excitation-contraction coupling. It is therefore not surprising that pathologies of the L-type Ca^{2+} channel can lead to abnormal Ca^{2+} dynamics. When we increase the single channel Ca^{2+} current i_{Ca}, subcellular Ca^{2+} alternans are more likely to occur as evidenced by the transition from blue to yellow in Fig. 6. However, this behaviour depends on the strength of Ca^{2+}-dependent inactivation of the L-type Ca^{2+} channel. As is often the case, the inactivation gate is modelled via a first-order kinetic scheme with a time constant τ_q and a state-dependent steady state q_∞. As Eq. (4) shows, q_∞ follows an inverse Hill function with exponent γ. Hence, for small values of γ, q_∞ changes gradually

as a function of the subsarcolemmal Ca^{2+} concentration c_s. On the other hand, large values of γ lead to a switch-like Hill function. When i_{Ca} is small, the increase in subsarolemmal Ca^{2+} is small as well, which in turn almost completely eliminates Ca^{2+} dependent inactivation (as q never falls sufficiently towards zero). Therefore, we do not observe any effect of γ on the generation of subcellular Ca^{2+} alternans in this regime, indicated by the blue band towards the left of Fig. 6. On the other hand, as we increase i_{Ca}, the larger subsarcolemmal Ca^{2+} concentrations allow for a larger exploration of the right tail of q_∞, and hence values closer to zero. When γ is large making q_∞ more steplike, bigger values of c_s^μ entail longer periods where q tends to zero. An increase of i_{Ca} does not change that, meaning that the nature of the subcellular Ca^{2+} alternans is not affected by increasing i_{Ca} for larger values of γ. This explains the almost uniform yellow colouring in Fig. 6 for fixed large γ and varying i_{Ca}. An interesting feature of Fig. 6 is the sharp transition from regular behaviour to subcellular Ca^{2+} alternans as is manifest from the abrupt colour change from blue to yellow. It remains to be seen whether this behaviour can be understood more formally in terms of a phase transition.

All results for the L-type Ca^{2+} channel were obtained with constant buffer contributions. However, since the concentration of Ca^{2+} bound buffers directly depends on the intracellular Ca^{2+} concentration, the buffer function β in Eq. (7) should evolve over time. Using the full nonlinear buffers, we find that subcellular Ca^{2+} alternans are extinguished (Fig. 7A). In other words, solely changing the buffer dynamics completely alters the dynamics of the cardiac cell. These findings are in line with a large body of literature demonstrating that Ca^{2+} buffers can substantially modify intracellular Ca^{2+} dynamics. From a physiological perspective, our results indicate that Ca^{2+} buffers can perform a stabilising role that can compensate for dysfunctions of other components of the Ca^{2+} signalling toolkit, such as the L-type Ca^{2+} channel. Because Ca^{2+} buffers are slaved to the Ca^{2+} dynamics, the buffer dynamics exhibit alternans as soon as the intracellular Ca^{2+} concentration alternates. For the results in Fig. 9, we broke this connection and clamped the Ca^{2+} buffer dynamics in such a way that each node exhibits the same nonlinear orbit. In other words, Ca^{2+} buffers alternate at each node, but there is no spatial variation of the buffer dynamics. In this regime, the patterns of the subcellular Ca^{2+} alternans vary drastically from the ones we observed so far. We found spatially concordant alternans, which can transition into spatially discordant alternans upon altering the coupling strength of cytosolic and SR diffusion. While we employed buffers to induce this pattern change, it is conceivable that such dynamics could originate from other dynamical variables of cardiac Ca^{2+} cycling. In this case, our results point to more subtle dependencies in that the nonlinear dynamics of cardiac Ca^{2+} cycling can be easily disturbed into new dynamic regimes, potentially inducing a plethora of cardiac arrhythmias. It is therefore astonishing that cardiac Ca^{2+} dynamics more often than not behaves completely regularly; a fact that certainly deserves more attention.

We first reported the emergence of subcellular Ca^{2+} alternans via a saddle-node bifurcation in a PWL caricature of an established Ca^{2+} cycling model [15]. One might wonder if this novel form of subcellular Ca^{2+} alternans is a consequence of the approximations used in the derivation of the PWL model. The results presented here show that this is not the case. The fully nonlinear model exhibits the same instabilities. This provides further evidence that PWL models are valuable in exploring the behaviour of complex nonlinear systems and thus adds to earlier success stories such as the McKean model, which represents a PWL version of the Fitzugh-Nagumo model for the propagation of neural action potentials [57–59]. The advantage of PWL models is that the majority of the analysis can be performed semi-analytically, which greatly facilitates the exploration of the associated parameter space. In turn, this allows for a more comprehensive classification of the possible dynamics. In contrast, fully nonlinear systems can often only be dissected via direct numerical simulations, which is often only done for a small subset of parameter values. In this respect, PWL models can provide guidance for the analysis of the nonlinear systems and where to explore in parameter space for interesting behaviour.

The last point becomes especially pertinent for the exploration of the different spatial patterns that emerge via a saddle-node bifurcation. As Figs. 2, 3, 7 and 9 illustrate, the Ca^{2+} profiles across the network exhibit significant variability. In a PWL model, these patterns can be classified and understood from a linear stability analysis, which can be performed in closed form [15,16]. On the other hand, the nonlinear model requires direct simulations, which are computationally more expensive and limited in scope as to what parameter values to sample.

Our model is based on the Shiferaw-Karma model [34], which is purely deterministic. Due to the small number of RyRs and L-type Ca^{2+} channels per CRU, hybrid models have been developed in which Ca^{2+} diffusion between adjacent CRUs is deterministic, but the dynamics of RyRs and L-type Ca^{2+} channels are described by Markov chains, rendering their behaviour stochastic. These models have been very successful in explaining the emergence of subcellular Ca^{2+} alternans via e.g. the 3R theory or an order-disorder transition, where the latter makes contact with phase transitions in the Ising model for ferromagnetism [6,7,60,61]. An interesting questions therefore arises in how far results from a purely deterministic model can accurately describe the (patho)physiology of a fluctuation-driven biological system. This discussion is central to the study of intracellular Ca^{2+} dynamics. As a case in point, consider the ongoing debate on modelling Ca^{2+} dynamics mediated by the inositol-1,4,5-trisphosphate receptor [62–67]. The power of deterministic models is often seen in providing a baseline for comparison with stochastic/hybrid models. In other words, to fully appreciate the impact that molecular fluctuations have on emergent cellular dynamics, we need to ascertain how models behave in their absence. This philosophy guided us in the present study, and it will be an exciting avenue for future research to determine how stochastic gating dynamics of RyRs and L-type Ca^{2+} channels modulate the results reported here.

Our study explores the emergence of subcellular Ca^{2+} alternans in a ventricular myocyte with severely impaired cytosolic Ca^{2+} diffusion and where Ca^{2+} transport occurs mainly via the SR. This is reflected in the small coupling strengths $\sigma_c = 2\ s^{-1}$ and $\sigma_{sr} = 30\ s^{-1}$, corresponding to diffusion time scales $\tau_c = 500$ ms and $\tau_{sr} = 33$ ms, respectively. To put these numbers into context, it is worth comparing them with diffusion time scales in healthy conditions. Care must be taken here

since reported diffusion coefficients vary greatly. For instance, Chen-Izu et al. [68] report cytosolic diffusion coefficients of 150 $\mu m^2\ s^{-1}$ and 300 $\mu m^2\ s^{-1}$ for transversal and longitudinal diffusion, respectively. For the SR, values of 8 $\mu m^2\ s^{-1}$ and 60 $\mu m^2\ s^{-1}$ have been reported. Since diffusive timescales scale as (length scale)^2/diffusivity, we obtain values of 4ms (assuming a transverse separation of 0.8 μm) and 10.8 ms (assuming a longitudinal separation of 1.8 μm) for the cytosol. For the SR, we arrive at 40.5ms and 5.4ms if we use a longitudinal distance of 1.8 μm. Restrepo et al. [42] point out that these estimates are crude and need to be refined. Based on this, they use diffusive coupling strengths of around 3 ms in the cytosol, but for the nonjunctional SR, values of 24 ms (longitudinal) and 7 ms (transverse) are used.

As stated above, our focus here is on tubulated myocytes. However, Ca^{2+} alternans have also been observed in non-tubulated cells such as atrial myocytes and failing ventricular myocytes [69–75]. In these cells, L-type Ca^{2+} channels are only located at the cell periphery, where they trigger Ca^{2+} release from the SR through the RyR. A Ca^{2+} wave then propagates centripetally from the periphery via diffusion and Ca^{2+} induced Ca^{2+} release [76,77]. Conceptually, it therefore makes sense to distinguish junctional CRUs (that contain L-type Ca^{2+} channels) and non-junctional CRUs (that lack L-type Ca^{2+} channels). Due to the stronger reliance on Ca^{2+} diffusion, it will be interesting to explore how differences in the diffusive coupling between CRUs and the fact there are two classes of CRUs shape subcellular Ca^{2+} alternans and whether the bifurcation structure observed for tubulated myocytes carries over to non-tubulated ones. Answering this question will not only unravel further similarities or differences between tubulated and non-tubulated myocytes, it will also advance our understanding of atrial fibrillation, which is projected to become epidemic with an ageing population [78].

Acknowledgement

This work was supported by the Engineering and Physical Sciences Research Council [grant number EP/P007031/1].

References

[1] Adabag AS, Luepker RV, Roger VL, Gersh BJ. Sudden cardiac death: epidemiology and risk factors. Nat Rev Cardiol 2010;7(4):216–25.
[2] Diaz ME, Eisner DA, O'Neill SC. Depressed ryanodine receptor activity increases variability and duration of the systolic Ca^{2+} transient in rat ventricular myocytes. Circ Res 2002;91(7):585–93.
[3] Kockskämper J, Blatter LA. Subcellular Ca^{2+} alternans represents a novel mechanism for the generation of arrhythmogenic Ca^{2+} waves in cat atrial myocytes. J Physiol 2002;545(1):65–79.
[4] Cordeiro JM, Malone JE, Di Diego JM, Scornik FS, Aistrup GL, Antzelevitch C, et al. Cellular and subcellular alternans in the canine left ventricle. Am J Physiol Heart Circ Physiol 2007;293(6):H3506–16.
[5] Shiferaw Y, Karma A. Turing instability mediated by voltage and calcium diffusion in paced cardiac cells. Proc Natl Acad Sci USA 2006;103(15):5670–5.
[6] Rovetti R, Cui X, Garfinkel A, Weiss JN, Qu Z. Spark-induced sparks as a mechanism of intracellular calcium alternans in cardiac myocytes. Circ Res 2010;106(10):1582–91.
[7] Qu Z, Nivala M, Weiss JN. Calcium alternans in cardiac myocytes: order from disorder. J Mol Cell Cardiol 2013;58:100–9.
[8] Gaeta SA, Bub G, Abbott GW, Christini DJ. Dynamical mechanism for subcellular alternans in cardiac myocytes. Circ Res 2009;105(4):335–42.
[9] Gaeta SA, Krogh-Madsen T, Christini DJ. Feedback-control induced pattern formation in cardiac myocytes: a mathematical modeling study. J Theor Biol 2010;266(3):408–18.
[10] Gaeta SA, Christini DJ. Non-Linear dynamics of cardiac alternans: subcellular to tissue-level mechanisms of arrhythmia. Front Physiol 2012;3:157.
[11] Restrepo JG, Karma A. Spatiotemporal intracellular calcium dynamics during cardiac alternans. Chaos 2009;19(3):037115.
[12] Aistrup GL, Shiferaw Y, Kapur S, Kadish AH, Wasserstrom JA. Mechanisms underlying the formation and dynamics of subcellular calcium alternans in the intact rat heart. Circ Res 2009;104(5):639–49.
[13] Tian Q, Kaestner L, Lipp P. Noise-free visualization of microscopic calcium signaling by pixel-wise fitting. Circ Res 2012;111(1):17–27.
[14] Thul R, Coombes S. Understanding cardiac alternans: a piecewise linear modeling framework. Chaos 2010;20(4):045102.
[15] Veasy J, Lai YM, Coombes S, Thul R. Complex patterns of subcellular cardiac alternans. J Theor Biol 2019;478:102–14.
[16] Lai YM, Veasy J, Coombes S, Thul R. A master stability function approach to cardiac alternans. accepted 2019.
[17] Alvarez-Lacalle E, Cantalapiedra IR, Peñaranda A, Cinca J, Hove-Madsen L, Echebarria B. Dependency of calcium alternans on ryanodine receptor refractoriness. PLoS One 2013;8(2):e55042.
[18] Tomek J, Tomková M, Zhou X, Bub G, Rodriguez B. Modulation of cardiac alternans by altered sarcoplasmic reticulum calcium release: a simulation study. Front Physiol 2018;9:1306.
[19] Huertas MA, Smith GD, Gyorke S. Ca^{2+} Alternans in a cardiac myocyte model that uses moment equations to represent heterogeneous junctional SR Ca^{2+}. Biophys J 2010;99(2):377–87.
[20] Nivala M, Qu Z. Calcium alternans in a couplon network model of ventricular myocytes: role of sarcoplasmic reticulum load. Am J Physiol Heart Circ Physiol 2012;303(3):H341–52.
[21] Qu Z, Liu MB, Nivala M. A unified theory of calcium alternans in ventricular myocytes. Sci Rep 2016;6:35625.
[22] Díaz ME, O'Neill SC, Eisner DA. Sarcoplasmic reticulum calcium content fluctuation is the key to cardiac alternans. Circ Res 2004;94(5):650–6.
[23] Li Y, Díaz ME, Eisner DA, O'Neill S. The effects of membrane potential, SR Ca^{2+} content and RyR responsiveness on systolic Ca^{2+} alternans in rat ventricular myocytes.. J Physiol 2009;587(Pt 6):1283–92.
[24] Swietach P, Spitzer KW, Vaughan-Jones RD. Ca^{2+}-mobility in the sarcoplasmic reticulum of ventricular myocytes is low. Biophys J 2008;95(3):1412–27.
[25] Picht E, Zima AV, Shannon TR, Duncan AM, Blatter LA, Bers DM. Dynamic calcium movement inside cardiac sarcoplasmic reticulum during release. Circ Res 2011;108(7):847–56.
[26] Bers DM, Shannon TR. Calcium movements inside the sarcoplasmic reticulum of cardiac myocytes. J Mol Cell Cardiol 2013;58(1):59–66.
[27] Bers DM. Cardiac excitation-contraction coupling.. Nature 2002;415(6868):198–205.
[28] Faber GM, Silva J, Livshitz L, Rudy Y. Kinetic properties of the cardiac L-type Ca^{2+} channel and its role in myocyte electrophysiology: a theoretical investigation.. Biophys J 2007;92(5):1522–43.
[29] Shaw RM, Colecraft HM. L-type calcium channel targeting and local signalling in cardiac myocytes. Cardiovasc Res 2013;98(2):177–86.
[30] Eisner DA, Caldwell JL, Kistamás K, Trafford AW. Calcium and excitation-contraction coupling in the heart. Circ Res 2017;121(2):181–95.
[31] Edwards JN, Blatter LA. Cardiac alternans and intracellular calcium cycling. Clin Exp Pharmacol Physiol 2014;41(7):524–32.
[32] Mahajan A, Sato D, Shiferaw Y, Baher A, Xie L-H, Peralta R, et al. Modifying L-type calcium current kinetics: consequences for cardiac excitation and arrhythmia dynamics. Biophys J 2008;94(2):411–23.
[33] Sato D, Dixon RE, Santana LF, Navedo MF. A model for cooperative gating of L-type Ca^{2+}channels and its effects on cardiac alternans dynamics. PLoS Comput Biol 2018;14(1):e1005906.

[34] Shiferaw Y, Watanabe MA, Garfinkel A, Weiss JN, Karma A. Model of intracellular calcium cycling in ventricular myocytes. Biophys J 2003;85(6):3666–86.
[35] Josephson IR, Guia A, Lakatta EG, Lederer WJ, Stern MD. Ca^{2+}-dependent components of inactivation of unitary cardiac L-type Ca^{2+} channels. J Physiol 2010;588(Pt 1):213–23.
[36] Grandi E, Morotti S, Ginsburg KS, Severi S, Bers DM. Interplay of voltage and Ca-dependent inactivation of L-type Ca current. Prog Biophys Mol Biol 2010;103(1):44–50.
[37] Smith GL, Eisner DA. Calcium buffering in the heart in health and disease. Circulation 2019;139(20):2358–71.
[38] Alvarez-Lacalle E, Penaranda A, Cantalapiedra IR, Hove-Madsen L, Echebarria B. Effect of RyR2 refractoriness and hypercalcemia on calcium overload, spontaneous release, and calcium alternans. In: Computing in cardiology 2013. IEEE; 2013. p. 683–6.
[39] Hake J, Edwards AG, Yu Z, Kekenes-Huskey PM, Michailova AP, McCammon JA, et al. Modelling cardiac calcium sparks in a three-dimensional reconstruction of a calcium release unit. J Physiol Lond 2012;590(Pt 18):4403–22.
[40] Kornyeyev D, Petrosky AD, Zepeda B, Ferreiro M, Knollmann B, Escobar AL. Calsequestrin 2 deletion shortens the refractoriness of Ca^{2+} release and reduces rate-dependent Ca^{2+}-alternans in intact mouse hearts. J Mol Cell Cardiol 2012;52(1):21–31.
[41] Stevens SCW, Terentyev D, Kalyanasundaram A, Periasamy M, Gyorke S. Intra-sarcoplasmic reticulum Ca^{2+} oscillations are driven by dynamic regulation of ryanodine receptor function by luminal Ca^{2+} in cardiomyocytes. J Physiol 2009;587(Pt 20):4863–72.
[42] Restrepo JG, Weiss JN, Karma A. Calsequestrin-mediated mechanism for cellular calcium transient alternans. Biophys J 2008;95(8):23.
[43] Lee Y-SY, Keener JPJ. A calcium-induced calcium release mechanism mediated by calsequestrin. J Theor Biol 2008;253(4):12.
[44] Terentyev D, Kubalova Z, Valle G, Nori A, Vedamoorthyrao S, Terentyeva R, et al. Modulation of SR Ca release by luminal Ca and calsequestrin in cardiac myocytes: effects of CASQ2 mutations linked to sudden cardiac death. Biophys J 2008;95(4):2037–48.
[45] Gyorke S, Terentyev D. Modulation of ryanodine receptor by luminal calcium and accessory proteins in health and cardiac disease. Cardiovasc Res 2008;77(2):245–55.
[46] Shannon TR. Linking calsequestrin to lumenal control of SR Ca^{2+} release. Circ Res 2007;101(6):539–41.
[47] Beard NAN, Laver DRD, Dulhunty AFA. Calsequestrin and the calcium release channel of skeletal and cardiac muscle. Prog Biophys Mol Biol 2004;85(1):37.
[48] Terentyev D, Viatchenko-Karpinski S, Györke I, Volpe P, Williams SC, Györke S. Calsequestrin determines the functional size and stability of cardiac intracellular calcium stores: mechanism for hereditary arrhythmia. Proc Natl Acad Sci USA 2003;100(20):11759–64.
[49] Wakili R, Yeh Y-H, Yan Qi X, Greiser M, Chartier D, Nishida K, et al. Multiple potential molecular contributors to atrial hypocontractility caused by atrial tachycardia remodeling in dogs. Circ Arrhythm Electrophysiol 2010;3(5):530–41.
[50] Dobrev D, Wehrens XHT. Calmodulin kinase II, sarcoplasmic reticulum Ca^{2+} leak, and atrial fibrillation. Trends Cardiovasc Med 2010;20(1):30–4.
[51] Yeh Y-H, Wakili R, Qi X-Y, Chartier D, Boknik P, Kääb S, et al. Calcium-handling abnormalities underlying atrial arrhythmogenesis and contractile dysfunction in dogs with congestive heart failure. Circ Arrhythm Electrophysiol 2008;1(2):93–102.
[52] Zalk R, Lehnart SE, Marks AR. Modulation of the ryanodine receptor and intracellular calcium. Annu Rev Biochem 2007;76:367–85.
[53] Jayasinghe I, Clowsley AH, de Langen O, Sali SS, Crossman DJ, Soeller C. Shining new light on the structural determinants of cardiac couplon function: insights from ten years of nanoscale microscopy. Front Physiol 2018;9(OCT):1472.
[54] Smith GD, Wagner J, Keizer J. Validity of the rapid buffering approximation near a point source of calcium ions. Biophys J 1996;70(6):2527–39.
[55] Wagner J, Keizer J. Effects of rapid buffers on Ca^{2+} diffusion and Ca^{2+} oscillations. Biophys J 1994;67(1):447–56.
[56] Petersen OH, Courjaret R, Machaca K. Ca^{2+} tunnelling through the ER lumen as a mechanism for delivering Ca^{2+} entering via store-operated Ca^{2+} channels to specific target sites. J Physiol 2017;595(10):2999–3014.
[57] McKean HP. Nagumo's equation. Adv Math 1970;4(3):209–23.
[58] FitzHugh R. Impulses and physiological states in theoretical models of nerve membrane. Biophys J 1961;1(6):445–66.
[59] Nagumo J, Arimoto S, Yoshizawa S. An active pulse transmission line simulating nerve axon. In: Proceedings of the IRE, 50; 1962. p. 2061–70.
[60] Cui X, Rovetti RJ, Yang L, Garfinkel A, Weiss JN, Qu Z. Period-doubling bifurcation in an array of coupled stochastically excitable elements subjected to global periodic forcing. Phys Rev Lett 2009;103(4):044102.
[61] Alvarez-Lacalle E, Echebarria B, Spalding J, Shiferaw Y. Calcium alternans is due to an order-disorder phase transition in cardiac cells. Phys Rev Lett 2015;114(10):108101.
[62] Falcke M, Moein M, Tilunaite A, Thul R, Skupin A. On the phase space structure of IP_3 induced Ca^{2+} signalling and concepts for predictive modeling. Chaos (Woodbury, NY) 2018;28(4):045115.
[63] Thul R. Translating intracellular calcium signaling into models. Cold Spring Harb Protoc 2014;2014(5).
[64] Thurley K, Skupin A, Thul R, Falcke M. Fundamental properties of Ca^{2+} signals. Biochim Biophys Acta 2012;1820(8):1185–94.
[65] Dupont G, Falcke M, Kirk V, Sneyd J. Models of calcium signalling. Interdisciplinary Applied Mathematics, 43. Springer; 2016.
[66] Sneyd J, Han JM, Wang L, Chen J, Yang X, Tanimura A, et al. On the dynamical structure of calcium oscillations. Proc Natl Acad Sci USA 2017;114(7):1456–61.
[67] Voorsluijs V, Dawson SP, De Decker Y, Dupont G. Deterministic limit of intracellular calcium spikes. Phys Rev Lett 2019;122(8):088101.
[68] Chen-Izu Y, McCulle SL, Ward CW, Soeller C, Allen BM, Rabang C, et al. Three-dimensional distribution of ryanodine receptor clusters in cardiac myocytes. Biophys J 2006;91(1):1–13.
[69] Song Z, Liu MB, Qu Z. Transverse tubular network structures in the genesis of intracellular calcium alternans and triggered activity in cardiac cells. J Mol Cell Cardiol 2017;114:288–99.
[70] Nivala M, Song Z, Weiss JN, Qu Z. T-tubule disruption promotes calcium alternans in failing ventricular myocytes: mechanistic insights from computational modeling. J Mol Cell Cardiol 2015;79:32–41.
[71] Chang KC, Bayer JD, Trayanova NA. Disrupted calcium release as a mechanism for atrial alternans associated with human atrial fibrillation. PLoS Comput Biol 2014;10(12):e1004011.
[72] Kanaporis G, Blatter LA. Alternans in atria: mechanisms and clinical relevance. Medicina (Kaunas, Lithuania) 2017;53(3):139–49.
[73] Lugo CA, Cantalapiedra IR, Peñaranda A, Hove-Madsen L, Echebarria B. Are SR Ca content fluctuations or SR refractoriness the key to atrial cardiac alternans?: insights from a human atrial model. Am J Physiol Heart Circ Physiol 2014;306:H1540–52.
[74] Florea SM, Blatter LA. Regulation of cardiac alternans by β-adrenergic signaling pathways. Am J Physiol Heart Circ Physiol 2012;303:H1047–56.
[75] Shkryl VM, Maxwell JT, Domeier TL, Blatter LA. Refractoriness of sarcoplasmic reticulum Ca^{2+} release determines Ca^{2+} alternans in atrial myocytes. Am J Physiol Heart Circ Physiol 2012;302(11):H2310–20.
[76] Thul R, Coombes S, Roderick HL, Bootman MD. Subcellular calcium dynamics in a whole-cell model of an atrial myocyte. Proc Natl Acad Sci USA 2012;109(6):2150–5.
[77] Bootman MD, Smyrnias I, Thul R, Coombes S, Roderick HL. Atrial cardiomyocyte calcium signalling. Biochim Biophys Acta 2011;1813(5):922–34.
[78] Morillo CA, Banerjee A, Perel P, Wood D, Jouven X. Atrial fibrillation: the current epidemic. J Geriatr Cardiol 2017;14(3):195–203.